


CrossMark
click for updates

Cite this: *RSC Adv.*, 2015, 5, 54649

Multi-scale simulation of non-equilibrium phase transitions under shear flow in dilute polymer solutions

Xin-Hai Xu, Xiao-Wei Guo,* Yu Cao, Xiao-Guang Ren, Juan Chen and Xue-Jun Yang

The phase transition of complex fluids is intrinsically a multi-scale problem. In this paper we propose a multi-scale two-fluid model that couples a coarse-grained microscopic method to the two-fluid framework for studying multi-phase fluids under shear flow. In this model the macroscopic viscoelastic stress is calculated by tracking the massive microscopic Brownian configuration fields in the simulation box. Both the macroscopic and microscopic equations are solved using a modified PISO iterative algorithm based on a finite volume discretization scheme. Our 2D numerical results reproduce numerous dynamic phenomena reported in literature and show that the theoretical model presented here could be a promising multi-scale approach to numerically study multi-phase viscoelastic fluids under flow.

Received 6th April 2015
Accepted 8th June 2015

DOI: 10.1039/c5ra06099k

www.rsc.org/advances

1 Introduction

Phase separation is a fundamental phenomenon that is commonly observed in complex fluids. Driven by the thermodynamical and viscoelastic forces the system can produce spatially heterogeneous patterns. After the experimental result presented by Silberberg¹ showing that the phase transitions of polymer solutions can be strongly influenced by flow, there have been numerous reports on the shear-induced phase separation in complex fluids.^{2–5} Typically, the morphology of the field will form into band structures under shear flow. As a closely related phenomenon, shear-banded flows also have been widely studied. The reader interested in shear-banding and its relations to the phase separation under shear flows may refer to the four review papers.^{6–9}

Although most of the numerical studies of shear-induced phase transitions considered the system in a thermal-equilibrium state, most systems found in nature are not in such an ideal state. In this paper we focus on non-equilibrium phase separation under shear flow. In classical binary fluids the spinodal decomposition will occur after a temperature quench without flow. This non-equilibrium phase separation has been well understood through numerous early experimental^{10–14} and numerical^{15–17} studies. Additionally, a number of intriguing effects induced by shear were observed, typical results included the highly elongated domains in very weak shear and a string phase in steady state under strong shear. For colloidal systems under shear the reader could refer to the review paper by Lowen.¹⁸ Stansell's group^{19,20} provided

convincing evidence for the non-equilibrium steady states through numerical simulation. Fielding²¹ presented an in-depth numerical study on the role of inertia in non-equilibrium steady states and confirmed that the non-equilibrium steady states free of finite-size effects only existed in systems with inertia.

Theoretically, modeling the phase transition under flow involves thermodynamics, hydrodynamics and viscoelastic effects. For simplicity, most of the previous studies about the non-equilibrium phase transition adopted a simple model ignoring the viscoelastic effects. As a macroscopic approach, the two fluid model^{22–25} was widely used to investigate phase separation in viscoelastic fluids. Numerous extensions^{26–29} of the original two-fluid model have been proposed recently and the results revealed that the model could capture the essential features of the viscoelastic phase separation. The two-fluid theoretical framework could be used to replace the previous simple models^{19–21} for studying the non-equilibrium viscoelastic phase separation.

Compared with classical viscous fluids, predicting the flow characteristics of a complex fluid is much more difficult since the macroscopic viscoelastic stress is determined by the complex microscopic dynamics of the molecular chains. This means that intrinsically the phase transition of complex fluids is a multi-scale problem. Atomistic modelling is the most detailed approach to describe rheological behaviour in complex fluids, however, considering the massive computer resource requirement, this microscopic approach is limited to flow geometries of molecular dimensions. Thus some micro-macro methods³⁰ were introduced that coupled the coarse-grained molecular kinetic theory to macroscopic continuum equations. The Brownian configuration field (BCF) method proposed by Hulsen *et al.*³¹ is a promising new multi-scale approach to

State Key Laboratory of High Performance Computing, National University of Defense Technology, China. E-mail: guoxiaowei@nudt.edu.cn

model viscoelastic fluids. The key idea of the BCF method is using Brownian configuration fields instead of tracking discrete particles, which significantly reduces the drawbacks of the CONFFESSIT method introduced by Laso and Ottinger.³² In practice the BCF method works very well and has been applied to simulations of numerous viscoelastic flows, including flows past a cylinder,^{31,33} viscoelastic free surface flows,³⁴ contraction and expansion flows,³⁵ Couette flows, Poiseuille flows, lid driven cavity flows³⁶ and flows between eccentrically rotating cylinders.³⁷ Due to the spatial smoothness, the BCF method has a considerable increased numerical stability. This advantage was confirmed in previous research and Mangoubi³⁸ recently gave an in-depth analysis about the origin of the numerical stability of the BCF method.

As a multi-scale approach, the BCF method requires much more computational resources compared to purely macroscopic approaches, both for CPU time and memory. Therefore, most simulations based on the BCF method are by now restricted to 2D spaces and homogeneous flow fields. The largest scale BCF simulation was presented by Griebel and Ruttgers,³⁹ in this study they produced the first 3D multi-scale FENE simulations using the BCF approach for square-square contraction flows. Nevertheless, to our best knowledge, there is so far no application of the BCF approach for simulations of viscoelastic phase transitions in complex fluids.

In this paper, we couple the BCF approach into the two-fluid framework and numerically solve this multi-scale two-fluid model through the finite volume method. We mainly focus on the 2D simulation results of the non-equilibrium phase separation phenomenon in dilute polymer solutions.

The remainder of the paper is organized as follows. In the next section the governing equations of a multi-scale two-fluid model are presented and the numerical algorithms for solving the equations are described in Section 2. Followed by the simulation results and discussions in Section 4. Section 5 contains our conclusions.

2 A multi-scale two-fluid model

For modeling the multi-phase fluid dynamics of a dilute polymer solution, we propose a multi-scale approach derived from the two-fluid concept and couple the Brownian Configuration Fields (BCF) method for computing the viscoelastic stress. The governing equations are divided into parts for the macroscopic and the microscopic description, respectively. At first, we give the Navier–Stokes equation and the evolution equation for the composition field at the macro-scale; subsequently, we specify the alternative approaches for calculating the stress tensor at the micro-scale involving stochastic differential equations.

2.1 Macroscopic equations

We consider the isothermal and incompressible fluid of a polymer solution with density ρ . From the macroscopic viewpoint, the motion of a polymer solution fluid can be governed by the continuity and the momentum balance equation:

$$\vec{\nabla} \cdot \vec{v} = 0 \quad (1)$$

and

$$\rho \frac{D\vec{v}}{Dt} = \eta_s \nabla^2 \vec{v} - \vec{\nabla} p - (2\phi_A - 1) \vec{\nabla} \mu + \vec{\nabla} \cdot \sigma_p(\vec{r}, t) \quad (2)$$

where the material derivative is $\frac{D\vec{v}}{Dt} = \frac{\partial \vec{v}}{\partial t} + \vec{v} \cdot \vec{\nabla} \vec{v}$. Involving the thermal and viscoelastic forces, the momentum balance equation is derived using Rayleigh's Variational Principle. For details the reader could refer to Onuki's publications.^{22,40} Here ϕ_A denotes the volume fractions of component A: the polymer solute, thus the fraction of the Newtonian solvent (component B) can be calculated as $\phi_B = 1 - \phi_A$. In eqn (2) \vec{v} and p are the volume average velocity of the fluid and the pressure field, respectively. η_s represents the solvent viscosity and σ_p is the time-dependent viscoelastic stress tensor contributed from the polymer dynamics. The viscoelastic stress term $\vec{\nabla} \cdot \sigma_p$ and the osmotic stress $\vec{\nabla} \mu$ are two significant contributions originating from the polymer chain dynamics and the thermodynamic effects, respectively. The thermodynamic effects in the two-fluid framework are described through the chemical potential difference $\mu = \mu_A - \mu_B$. The chemical potentials are approximately defined in the Ginzburg–Landau scheme,⁴⁰ thus μ is assumed to be the functional derivative of the mixing free energy with respect to the local volume fraction as

$$\mu = \frac{\delta \mathcal{F}_{\text{mix}}[\phi_A(\vec{r})]}{\delta \phi_A(\vec{r})} \quad (3)$$

We take a first order approximation of the Flory–Huggins–de Gennes mixing free energy function as

$$\mathcal{F}_{\text{mix}}[\phi_A(\vec{r})] = \int d\vec{r} \{ f_{\text{mix}} + (I/2) [\nabla \phi_A]^2 \} \quad (4)$$

and

$$f_{\text{mix}}/k_B T = (1/M_A) \phi_A \ln \phi_A + (1/M_B) \phi_B \ln \phi_B + \chi \phi_A \phi_B \quad (5)$$

where I is the interfacial tension coefficient, M_i is the molecular weight of each component polymer and χ is the Flory–Huggins interaction parameter.

The evolution equation for the volume fraction can be expressed as

$$\frac{D\phi_A(\vec{r}, t)}{Dt} = \vec{\nabla} \cdot \left[\frac{\phi_A^2 (1 - \phi_A)^2}{\zeta} (\vec{\nabla} \mu - \alpha \vec{\nabla} \cdot \sigma_p) \right] \quad (6)$$

which brings the osmotic stress and the viscoelastic stress terms together on the right of the equation. The parameter ζ is a frictional coefficient and α is a dimensionless coefficient given by $\alpha = \frac{1}{\phi_A}$.

The chemical potential difference can be calculated from eqn (3) and the total viscoelastic stress σ_p should be obtained by solving the constitutive equations. As Yuan⁴¹ argued that the tube velocity should be used in the viscoelastic constitutive equation, the tube velocity may be expressed in terms of the volume average velocity by

$$\vec{v}_T = \vec{v} + \phi_A(1 - \phi_A)\alpha(\vec{v}_A - \vec{v}_B) \quad (7)$$

$$\vec{v}_A - \vec{v}_B = \frac{\phi_A(1 - \phi_A)}{\zeta} \left[-\vec{\nabla}\mu + \alpha\vec{\nabla} \cdot \sigma_p \right] \quad (8)$$

As eqn (8) shows, the velocity difference between components A and B depends on the thermodynamic and viscoelastic forces. In this paper we aim to model a polymer solution where only one component (A) is viscoelastic and the tube velocity is simplified to $\vec{v}_T = \vec{v}_A$.

2.2 Microscopic equations

From a microscopic viewpoint we set up a FENE dumbbell model for the dilute polymer solution, where the molecular chain of the polymer is considered as a suspension dumbbell consisting of two separate Brownian beads connected with an elastic spring. Using a vector \vec{Q} to represent the length and the orientation of the connecting spring, the spring force can be written as the FENE form:

$$F(\vec{Q}) = \frac{\vec{Q}}{1 - |\vec{Q}|^2/b}, \quad |\vec{Q}| \leq b \quad (9)$$

where the parameter b gives the dumbbell a maximum extension.

The BCF method introduces N_f configuration fields $\vec{Q}_i(\vec{r}, t)$ to replace the Fokker-Planck equation for describing the configuration distribution. We rewrite the corresponding stochastic differential equation as³¹

$$d\vec{Q}_i(\vec{r}, t) = \left[-\vec{v}(\vec{r}, t) \cdot \nabla \vec{Q}_i(\vec{r}, t) + (\nabla \vec{v}(\vec{r}, t))^T \cdot \vec{Q}_i(\vec{r}, t) - \frac{F(\vec{Q}_i(\vec{r}, t))}{2\lambda(\phi_A)} \right] dt + \sqrt{\frac{1}{\lambda(\phi_A)}} d\vec{W}_i(t) \quad (10)$$

In this representation $d\vec{W}_i(t)$ only depends on time and essentially is an independent Gaussian variable with a zero mean and variance dt . Importantly the random variables are independent on the position \vec{r} . As discussed in Section 2.1, in this equation we should use the tube velocity calculated through eqn (7). To approximate the actual probability density function, we solve eqn (10) for a number of stochastic realizations, represented by $\vec{Q}_i(\vec{r}, t)$, $i = 1, 2, \dots, N_f$. According to the Kramers expression, the polymer contribution to the extra-stress σ_p can be given by³⁶

$$\sigma_p = \left(\frac{b + d + 2}{b} \right) \frac{\eta_p(\phi_A)}{\lambda(\phi_A)} \left(\langle \vec{Q} \otimes F(\vec{Q}) \rangle - I \right) \quad (11)$$

where the factor $(b + d + 2)/b$ only needs to be multiplied for the FENE model, and d is the dimension of the configuration space. Using a Monte Carlo integration the ensemble average $\langle \vec{Q} \otimes F(\vec{Q}) \rangle$ can be approximately calculated by

$$\langle \vec{Q} \otimes F(\vec{Q}) \rangle \approx \sum_{i=1}^{N_f} \vec{Q}_i(\vec{r}, t) \otimes F(\vec{Q}_i(\vec{r}, t)) \quad (12)$$

In polymer solutions, the relaxation time λ and the polymer viscosity η_p are dependent on the concentration. Here in eqn (10) and (11) we use two material functions, $\lambda(\phi_A)$ and $\eta_p(\phi_A)$, to describe their relations. For simplicity, we assume a power-law dependence⁴² of $\lambda(\phi_A) = \lambda^0 \phi_A^{1.5}$ and $\eta_p(\phi_A) = \eta_p^0 \phi_A^{2.25}$.

3 Numerical method

We use a PISO-based iterative solution algorithm to solve the multi-scale model. This algorithm has been well tested in a numerical study for the dynamics of polymer solutions in contraction flow.⁴³ Recently, it was adopted to study the shear-banding flows with a macroscopic two-fluid model.²⁹ Derived from the algorithm described in ref. 43, the chemical potential difference unknowns and the polymer stress unknowns are both explicitly introduced into the momentum equation as source terms, therefore eqn (2) could be rewritten as

$$\frac{\partial \vec{v}}{\partial t} + \vec{v} \cdot \nabla \vec{v} - \frac{\eta_s \nabla^2 \vec{v}}{\rho} + \frac{(2\phi_A - 1)}{\rho} \vec{\nabla} \mu - \frac{\vec{\nabla} \cdot \sigma_p(\vec{r}, t)}{\rho} = -\frac{\vec{\nabla} p}{\rho} \quad (13)$$

After discretizing through finite volume method, this equation can be abbreviated into a form of the linear system as

$$A\vec{v}^{n+1} = H^n - \nabla[p]^n \quad (14)$$

where the brackets $[\cdot]$ represent the numerical approximation of the unknown fields, the superscript n and $n + 1$ denote the value of the past and present times of the variable. The polymer stress contribution and the osmotic stress term are treated as the source terms and are contained in the symbol H^n . However, the viscous term and the convective term are implicitly discretized into the matrix A of the linear system. Multiplying eqn (14) by A^{-1} yields

$$\vec{v}^{n+1} = \vec{U}^{n+1} - A^{-1} \nabla[p]^n \quad (15)$$

where $\vec{U}^{n+1} = A^{-1} H^n$ is obtained by taking the divergence of eqn (15) and applying the continuity condition in eqn (1). We can get a Poisson equation by solving the pressure field in the pressure-correction step:

$$\nabla \cdot \vec{U}^{n+1} = \nabla \cdot (A^{-1} \nabla[p])^{n+1} \quad (16)$$

Eqn (15) and (16) define the key steps for the PISO algorithm. In this paper, we replace the constitutive equation part for solving the viscoelastic stress tensor to a microscopic BCF method. A semi-implicit Euler method³⁹ is employed to solve the equations of the Brownian configuration fields. Combining the two parts together, we get the procedure of the iterative algorithm for solving the multi-scale two-fluid model as Scheme 1.

In Scheme 1 $\vec{N}_i(0,1)$ denotes a vector containing a triple of independent Gaussian random variables with zero mean and variance one. To discretize the governing equations of the

Data: Mesh data, initial conditions

Result: \vec{v} , p , σ_p , ϕ_A

```

1 read the mesh data and the initial conditions;
2 initialization;
3 while  $t^{n+1}$  not reach the end of the simulation time do
4   for  $i = 1$  to  $N_f$  do
5     Solve eqn (10) to get the configuration field  $\vec{Q}_i(\vec{r}, t)$  at
      time  $t^{n+1}$  using a semi-implicit Euler method:
      
$$(1 + \frac{\Delta t^n}{2\lambda(\phi_A^n)(1-|\vec{Q}_i^{n+1}(\vec{r})|^2/b)})\vec{Q}_i^{n+1}(\vec{r}) = \vec{Q}_i^n(\vec{r}) + [-\vec{v}^n(\vec{r}) \cdot$$

      
$$\nabla \vec{Q}_i^n(\vec{r}) + (\nabla \vec{v}^n(\vec{r}))^T \cdot \vec{Q}_i^n(\vec{r}, t)]\Delta t^n + \sqrt{\frac{\Delta t^n}{\lambda(\phi_A^n)}}\vec{N}_i(0, 1);$$

6   end
7   Compute the polymer stress tensor using Kramers'
      expression
      
$$\sigma_p^{n+1}(\vec{r}) = (\frac{b+d+2}{b})\frac{\eta_p(\phi_A^n)}{\lambda(\phi_A^n)}(\sum_{i=1}^{N_f}\vec{Q}_i^{n+1}(\vec{r}) \otimes F(\vec{Q}_i^{n+1}(\vec{r})) - \mathbf{I});$$

8   Solve the discretised momentum equation (eqn (13)) to
      obtain the estimated components  $\vec{U}^{(n+1)*}$ ;
9   Solve the pressure-correction equation (eqn (16)) to
      obtain the pressure field  $p^{(n+1)*}$ ;
10  Calculate the corrected velocity field  $\vec{v}^{(n+1)*}$  by solving
      eqn (15);
11  Repeat the steps 8 ~ 10 using the corrected
       $p^{(n+1)*}$ ,  $\vec{v}^{(n+1)*}$  until all corrections are negligibly small for
      the solutions at the present time  $\vec{v}^{n+1}$  and  $p^{n+1}$ ;
12  Solve eqn (6) using  $\sigma_p^{n+1}$  and  $\vec{v}^{n+1}$  to obtain the volume
      fraction  $\phi_A^{n+1}$ ;
13   $n \leftarrow n + 1$ ;
14 end

```

Scheme 1 The iterative algorithm to solve the multi-scale two-fluid model.

multi-scale two-fluid model, eqn (1) to (12), we use an Open Source CFD toolbox released by the OpenCFD Ltd, named OpenFOAM. The equations are discretized through the finite volume method, which locally satisfied the physical conservation laws through computing each term of the governing equations by the integral over a control volume. For spatial discretization terms the 2nd-order Gauss MINMOD and Gauss Linear scheme are applied and the temporal terms are discretized using a simple Euler scheme. Finally these equations will reduce to linear systems, thus using the iterative solvers predefined in OpenFOAM we can get the solutions of the equations at every time step. Typical solvers in the toolbox include the conjugate (PCG) and biconjugate gradient (PBiCG) methods. For details please refer to the OpenFOAM Manual.

4 Results and discussions

In this section we focus on the two-dimensional simulation with a simulation box with square geometry, and the cell number is set to $N_{\text{cell}} = 256 \times 256$. The algorithm presented in Scheme 1 is parallelized by a mesh-decomposition approach. In principle, all of the mesh cells are firstly decomposed into numerous parts and then distributed to different processor cores for computing. Therefore all of the sections of the algorithm are calculated in parallel.

We run the simulations on a high performance computing cluster located in the State Key Laboratory of High Performance Computing of NUDT. In this cluster each computing node contains 12 Intel Xeon E5-2620 2.10 GHz CPU cores and a total main memory of 16 GB. Each calculation presented in the paper costs around 2 days to 7 days on 16 CPU cores depending on the shear rates.

The top and bottom boundaries are no-slip walls and a periodic boundary condition is applied to the other two sides of the simulation box. As presented in numerous previous studies,^{27,29} care has to be taken in all simulations to ensure that there are sufficient lattice sites (seven at least) across the sharpest interfaces and also that the simulation results are independent of any further refinement of the lattice density.

To apply a required shear rate $\dot{\gamma}$, a velocity with the magnitude of $U_0 = \dot{\gamma}(L/2)$ is set to the top and bottom walls in equal speed and opposite directions, where L is the distance between the walls. Other parameters remain constant throughout all of the simulations and are set as shown in Table 1.

For this set of parameters, the critical point is at ($\chi = 2.0$, $\phi_A^0 = 0.5$), as shown in Fig. 1. By changing the value of χ and the initial volume fraction ϕ_A^0 , different regions in the phase diagram can be explored. For simplicity, in this paper we fix the initial volume fraction $\phi_A^0 = 0.5$ for studying a symmetric binary fluid and $\phi_A^0 = 0.3$ for an asymmetric case.

In the simulations, we employ the 2D FENE dumbbell model to predict the viscoelastic stress of a shear-shinning fluid. Compared to the simple Hookean dumbbell model, the extensibility parameter b controls the fluid's shear thinning behaviour. As shown in numerous publications,^{39,44,45} the steady-state numerical results of the stress varied significantly by changing the value of b . To give a preliminary validity of the numerical scheme presented in Section 3, we performed the steady shear flow simulations with fixed Weissenberg Number $W_e = \dot{\gamma}\lambda \in [1, 103]$, and by setting the cell number of the mesh $N_{\text{cell}} = 1$ the spatial discretization is neglected. For a fixed W_e , each simulation evolved $N_f = 50\,000$ Brownian Configuration fields until a steady state was reached. Thus we can measure the resulting stresses and finally give the value of the total viscosity of the fluid, η_t , and the shear stress for the corresponding W_e .

The results are presented in Fig. 2. The viscosity η_t in Fig. 2(a) decreases with W_e increasing. This typical shear-shinning behaviour was observed experimentally in polymer solutions⁴⁶ and compared numerically using a macroscopic PTT

Table 1 Parameters used in simulations

Parameter	Value
η_s	0.1
$k_B T$	1.3
M_A	1.0
M_B	1.0
Γ	1.0
ζ	0.1
b	20.0
λ^0	10.0
η_p^0	20.0

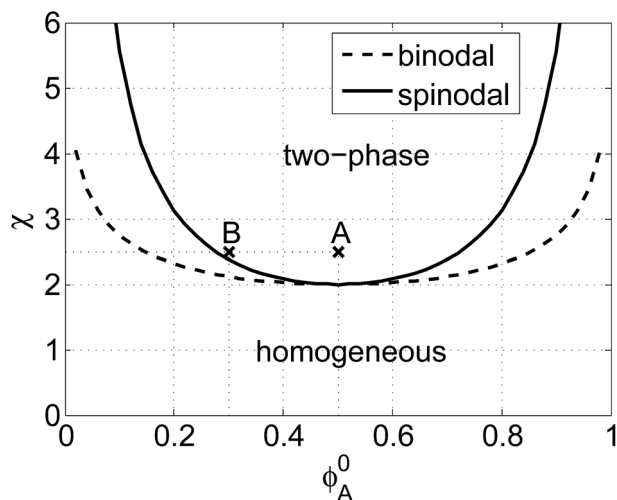


Fig. 1 Equilibrium phase diagram of the Flory-Huggins free energy with parameters: $M_A = M_B = 1.0$ and $k_B T = 1.3$. The homogeneous and two-phase fluid areas are bordered by binodal and spinodal lines, and between the two is a metastable region. The two bold crosses mark the parameters used in this paper: (A) $(\phi_A^0, \chi) = (0.5, 3.0)$ and (B) $(\phi_A^0, \chi) = (0.3, 3.0)$.

constitutive model and a multi-scale model coupling the BCF scheme.³⁹ The corresponding constitutive curves are presented in Fig. 2(b). All the curves follow similar trends and the larger extensibility lead to greater stresses as shown in the results. In practice the maximum Weissenberg number achievable reduces as b increases. As pointed by Chauviere,⁴⁴ increased b means that the configuration domain becomes larger, therefore more refined meshes would be necessary in order to capture localized features. We chose a moderate value of the extensibility, $b = 20$, for all the simulations below.

For the convergence study, we compared the simulation results with the steady-state solutions in Fig. 2 under different mesh widths and various numbers of configuration fields, N_f . The time step size is restricted by the CFL condition $\Delta t \leq \Delta x / |u_{\max}|$ in our simulations. The results are presented in Fig. 3. For a constant $N_f = 500$, the truncation error for the steady-state shear stress is linearly decreased with an increasing number of cells. Differently, with a fixed mesh size $N_{\text{cell}} = 256^2$, the error is rapidly reduced to around 10^{-2} as N_f increased to 500, however there is no significant variation from $N_f = 500$ to $N_f = 3000$. Considering the massive computing resource requirements for large N_f , we chose $N_f = 500$ for all the simulations presented below.

Without shear flow, the phase separation will spontaneously take place after a deep temperature quench and the fluid will form into a two-phase state driven by the thermodynamical forces. The asymmetry between the components of the polymer mixtures can also strongly change the morphology of the phase separation.^{41,47} Typically, in the zero-shear system an asymmetric quench can lead to a droplet pattern, differently from the bicontinuous pattern for a nearly symmetric quench.⁴⁸ In order to reproduce the spinodal decomposition process in a zero-shear system, we carry out two sets of simulations with a

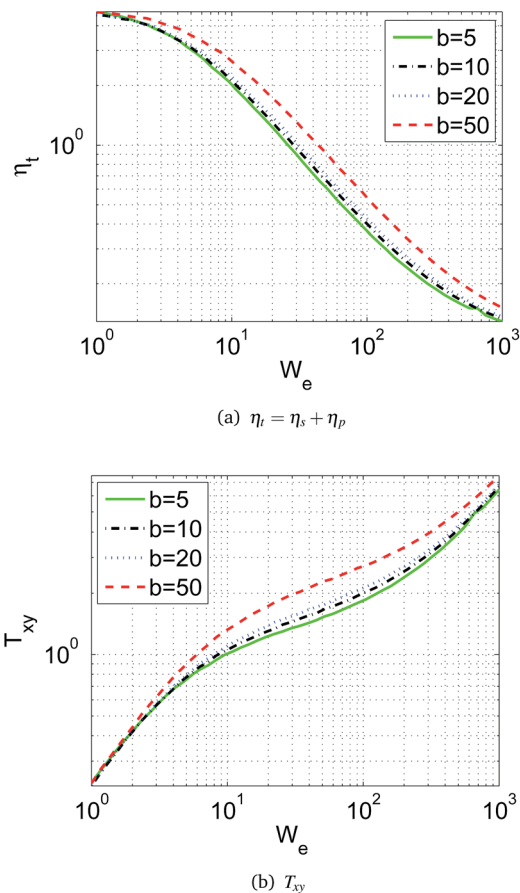


Fig. 2 The scaled steady-state shear stress (scaled by $\frac{\eta_p^0}{\lambda^0}$) and the total viscosity over W_e with $b = 5, 10, 20, 50$ for $N_f = 50\,000$.

symmetric initial composition $\phi_A^0 = 0.5$ and an asymmetric initial composition $\phi_A^0 = 0.3$. The time series of the numerical results are presented in Fig. 4 and 5.

Fig. 4 shows the snapshots of the composition field ϕ_A for the critical quench $\phi_A^0 = 0.5$. At $t = 6\lambda$, the clearly isotropic bicontinuous domain structure has been formed and the difference between the two phases grows as the phase separation proceeds. The coarsening of the morphology structure with

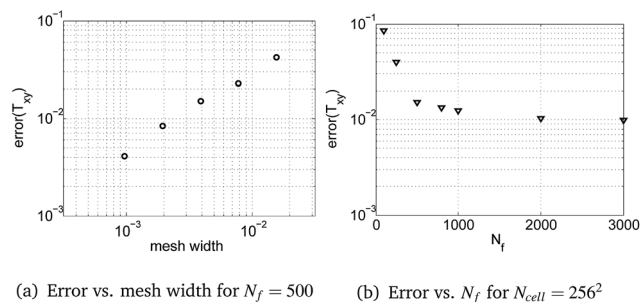


Fig. 3 The convergence study with different mesh widths and numbers of configuration fields. The $\text{error}(T_{xy})$ is calculated through the steady-state truncation error of the shear stress normalized by the results for $N_{\text{cell}} = 1$.

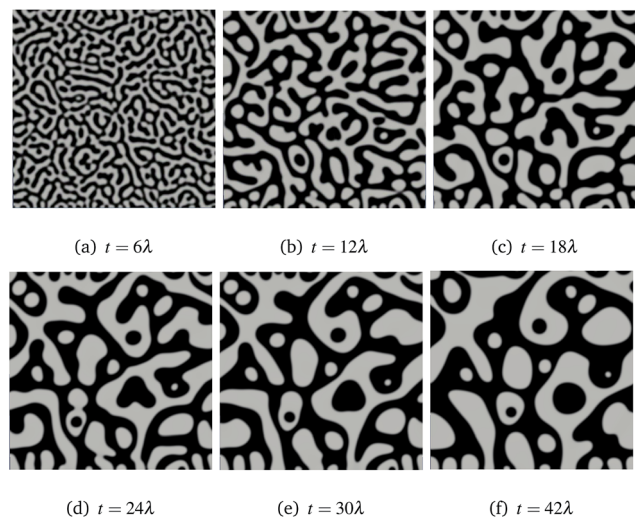


Fig. 4 Time series of the phase separation after a deep quench into the spinodal region through the symmetric initial composition $\phi_A^0 = 0.5$ and $\chi = 2.5$.

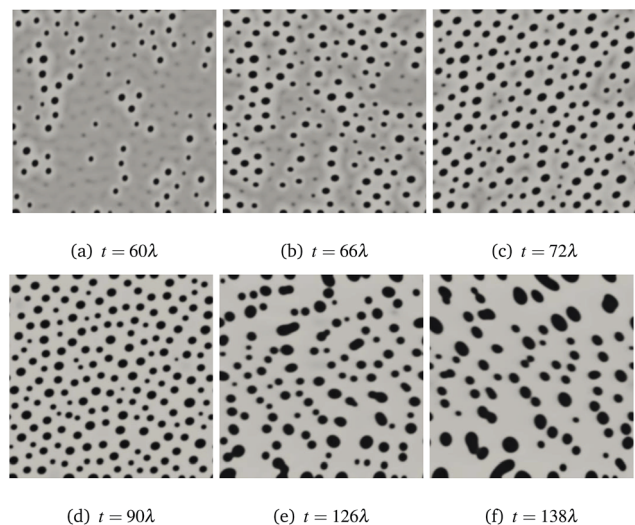


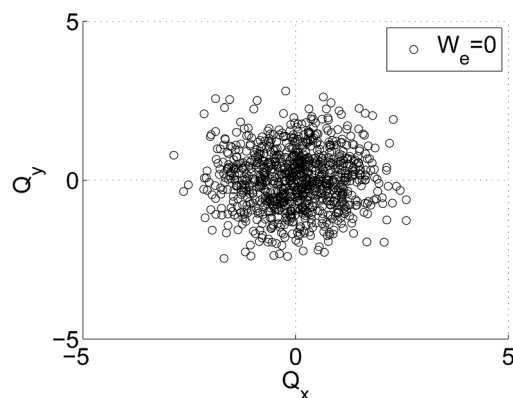
Fig. 5 Time series of the phase separation after a deep quench into the spinodal region at an asymmetric initial composition $\phi_A^0 = 0.3$ and $\chi = 2.5$.

time can be clearly seen from the plots. After $t = 50\lambda$, the finite-size effects can not be eliminated and therefore the full hydrodynamic regime is not obtainable. Fig. 5 is the time series of snapshots for the asymmetric case with $\phi_A^0 = 0.3$. Differently, the polymer-rich phase (component A) forms a dispersed droplet structure. As the simulation proceeds, the smallest droplets dissolve completely into the continuous solvent phase and the larger droplets merge together, thus the average size of the droplets increases with time.

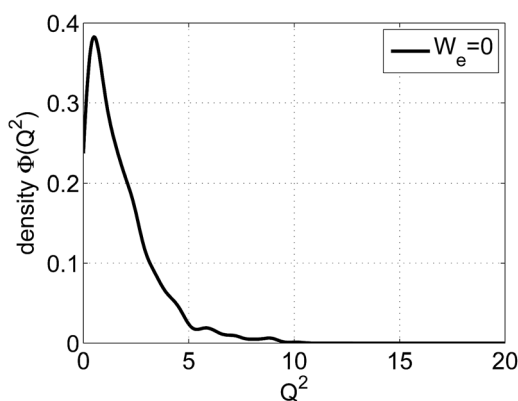
From a microscopic viewpoint, we plot the polymer configurations at the position (64, 64) in Fig. 6. After visualizing the configuration vectors in Fig. 6(a), the probability density function (PDF) for the squared distance \vec{Q}^2 which is limited by $b = 20$

is calculated. From the plots it is clear that most of the configurations are in an equilibrium state in the absence of flow and no significant molecule extension is found as shown in Fig. 6(b).

For the cases with the fluid under different flow rates, firstly the simulation results for the homogeneous cases ($\chi = 1.0$, $\phi_A^0 = 0.5$) and the two-phase cases ($\chi = 2.5$, $\phi_A^0 = 0.5$) are plotted in Fig. 7, along with the corresponding steady-state shear stress with $N_{\text{cell}} = 1$. For this set of parameters, the constitutive curve calculated from the microscopic Brownian configurations is strictly monotonic as indicated in Fig. 7. Additionally for the homogeneous cases, the simulation results using the numerical algorithms described in Section 3 coincide well with the steady-state calculations. Whilst the phase separation occurs by changing the parameter $\chi = 2.5$, the calculated shear stresses are markedly smaller than the homogeneous cases. This observation coincides with the numerical results based on a macroscopic constitutive model.²⁹ We also tested different numbers of the Brownian configurations, and it was observed that a larger N_f will bring a higher accuracy to the calculations. Considering the simulation time cost, we chose $N_f = 500$, and it was found that the results are generally satisfactory as shown in Fig. 7.



(a) The vector \vec{Q}



(b) The PDF of \vec{Q}^2

Fig. 6 The distribution of the configuration vectors sampled at the position (64, 64) with $N_f = 500$ in a zero-shear system.

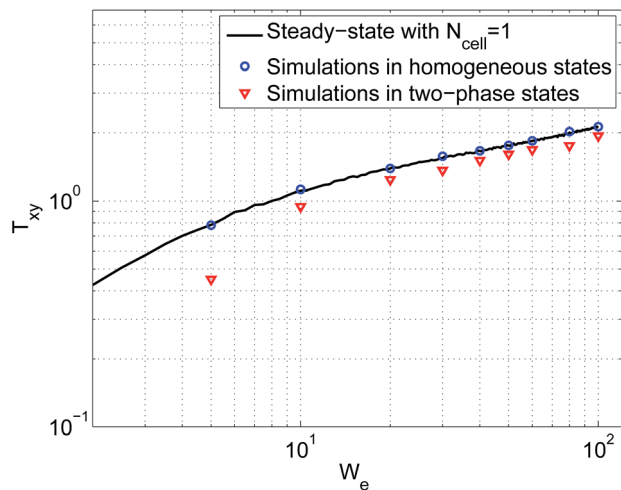


Fig. 7 The scaled steady-state shear stress with $N_{\text{cell}} = 1$, $N_f = 5 \times 10^4$ and the simulation results for the homogeneous cases ($\chi = 1.0$, $\phi_A^0 = 0.5$) and the two-phase cases ($\chi = 2.5$, $\phi_A^0 = 0.5$) under different flow rates with $N_f = 500$.

By applying the shear flow, the phases will be rapidly elongated and form into band structures. As shown in Fig. 8 for the case of $W_e = 20.0$, snapshots of the composition field at several instants during the spinodal phase separation give us the detailed information for the microstructure evolution driven by thermodynamics, hydrodynamics and viscoelasticity. At the beginning point, $t = 0$, the fluids are defined on a completely homogeneous volume fraction plus a small amplitude Gaussian random noise with an intensity of 10^{-3} . As shown in Fig. 8(b) and (c), shear bands emerge rapidly and become coarser through a diffusive mechanism. After $t = 5.4\lambda$, the wavy structures between the bands have become extremely unstable and have begun to evolve in a chaotic manner. At later times

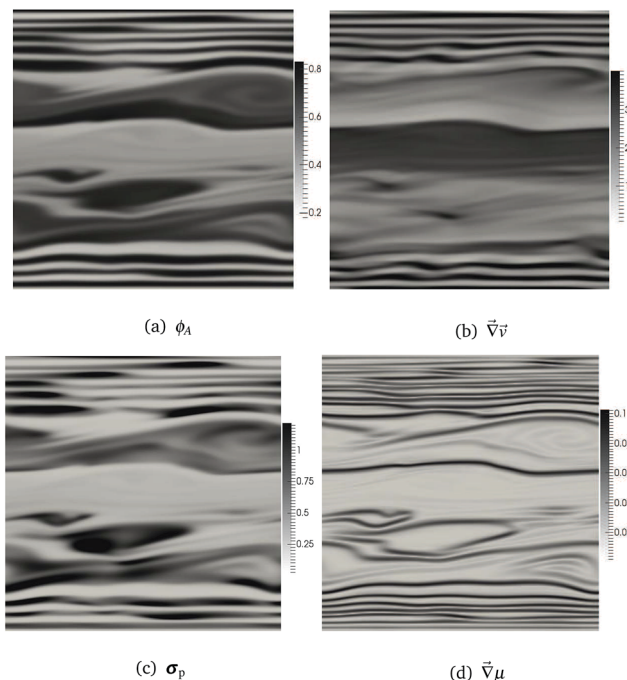


Fig. 9 The snapshots of field variables at the same time $t = 35\lambda$.

presented in Fig. 8(g)–(l), it is observed that the wavy structures break up to form droplets, then the droplet interacts with the remaining bands and subsequently forms into a coarser band. Overall, the dynamical mechanisms by which the shear bands reach the steady state are analogous to the phenomena reported in thermodynamical equilibrium shear-banding systems.^{27,29,41} One is the diffusive mechanism and the another is the convective through wave instability. By introducing the thermodynamical forces in a two-phase region of the phase diagram, the shear bands are becoming much more

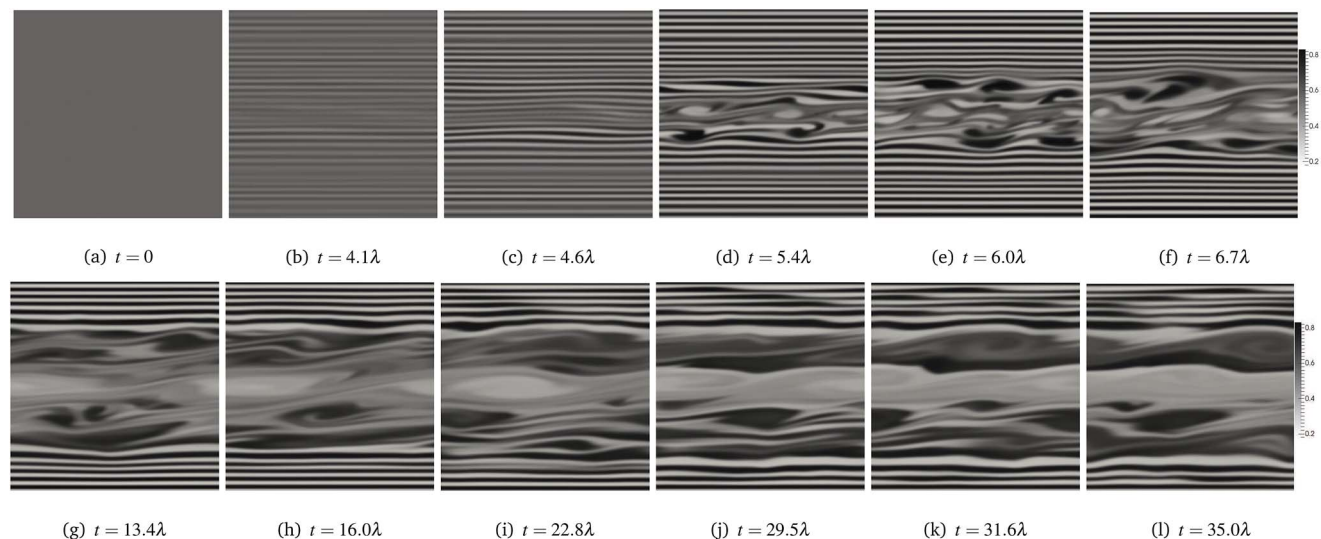


Fig. 8 The snapshots of the composition field of the polymer component at various times t , scaled by the relaxation time λ for the case of $W_e = 20$.

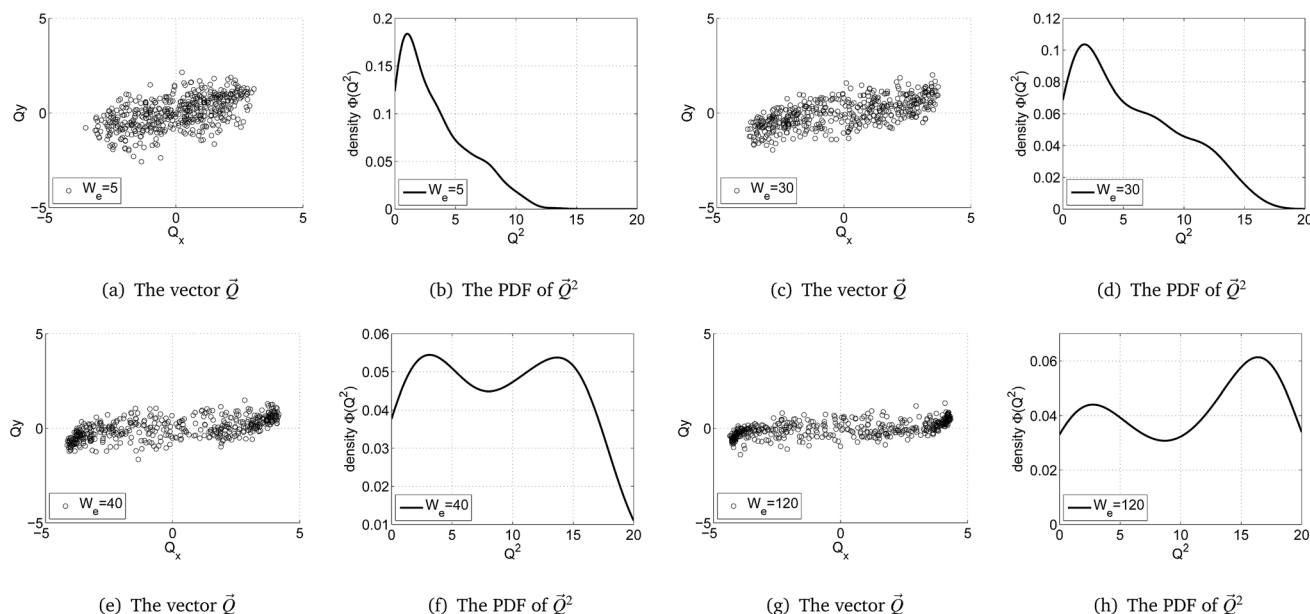


Fig. 10 The distribution of the molecule configurations with $N_f = 500$ under different shear flows at the lattice point (64, 64).

unstable and can not reach a steady state for a long simulation time.

It is clear that the phase separation is directly linked to the rheological properties of the fluid and the applied flow field. As presented in Fig. 9, the evolution of the gradient of the velocity field and the stress field follow similar patterns to those of the composition field. In Fig. 9(b) and (c), the $\nabla \vec{v}$ and sigp form into similar band structures as Fig. 9(a) at $t = 35\lambda$. From Fig. 9(d) we can tell that the osmotic pressure field $\nabla \mu$ introduces an interfacial force concentrating at the narrow interfaces between the polymer-rich region and the solvent-rich region.

To explore the distribution of the molecule configurations under different shear flows, we recorded the configuration fields at the lattice point (64, 64) for four different Weissenberg numbers. As shown in Fig. 10, the corresponding PDF calculations have also been plotted in the right column of the figure. For the case with a low shear rate $We = 5$, the molecule chains are obviously elongated compared to the zero-shear case shown in Fig. 6. In absence of flow, most of configurations are restricted to the range of $\vec{Q}^2 < 5$, yet in Fig. 10(a) and (b), a considerable amount of molecules have been stretched and the measurement of \vec{Q}^2 increased to the range of $[5, 10]$. Under a much higher shear flow for $We = 120$ shown in Fig. 10(g) and (h), most of the sampled molecules are extremely elongated close to their maximum as $10 < \vec{Q}^2 < 20$. From the plots for four different Weissenberg numbers, we obtained a typical shear flow pattern for both flows as the higher shear flows lead to stronger molecule extensions.

5 Conclusions

The phase transitions under flow have been extensively studied experimentally and numerically over the last decades, nevertheless, due to the massive computational requirements, there

are still no multi-scale numerical studies that link the microscopic molecule configurations to the macroscopic morphological transitions in multi-phase fluids under flow. As a coarse-grained microscopic approach, the Brownian Configuration Fields (BCF) method makes it possible to model the macroscopic phenomena of complex fluid from a microscopic viewpoint.

In this paper we coupled the BCF method to a two-fluid framework to model the phase transition under shear flow in dilute polymer solutions. The governing equations are solved using a modified PISO iterative algorithm based on the finite volume scheme. Based on necessary validations, 2D simulation results of non-equilibrium phase transitions after a temperature quench under shear flow were presented and analyzed. From a macroscopic viewpoint, we gave the time series of the morphological evolution of the macroscopic variable fields, and the results reproduced many dynamic phenomena reported in literature, including the spinodal decomposition, the interface instabilities between the shear bands and the dynamic mechanisms to reach coarser band structures. From a microscopic viewpoint, the distribution of the molecule configurations in the simulation box could be observed as the phase transition taking place. The underlying configuration fields were recorded and the corresponding PDFs were analyzed under various flow rates.

The multi-scale two-fluid model presented here provides a possible approach to numerically study multi-phase viscoelastic fluids under flow. In the future, this model could be used to quantitatively study some outstanding problems by appropriately selecting the parameters based on experimental observations. Furthermore, we will optimize the parallel algorithms to significantly reduce the computational costs.

Acknowledgements

The authors would like to thank Prof. Xue-Feng Yuan for helpful discussions, the National Natural Science Foundation of China (Grant no. 61221491, 61303071 and 61120106005) and the Open fund from State Key Laboratory of High Performance Computing (no. 201303-01, 201503-01 and 201503-02) for funding.

References

- 1 A. Silberberg and W. Kuhn, *Nature*, 1952, **170**, 450–451.
- 2 S. Ravindranath, S. Q. Wang, M. Olechnowicz, V. S. Chavan and R. P. Quirk, *Rheol. Acta*, 2011, **50**, 97–105.
- 3 S. Lerouge and J. F. Berret, *Polymer Characterization: Rheology, Laser Interferometry, Electrooptics*, 2010, **230**, 1–71.
- 4 M. Laurati, G. Petekidis, N. Koumakis, F. Cardinaux, A. B. Schofield, J. M. Brader, M. Fuchs and S. U. Egelhaaf, *J. Chem. Phys.*, 2009, **130**, 134907.
- 5 B. Lonetti, M. Camargo, J. Stellbrink, C. N. Likos, E. Zaccarelli, L. Willner, P. Lindner and D. Richter, *Phys. Rev. Lett.*, 2011, **106**, 228301.
- 6 P. D. Olmsted, *Rheol. Acta*, 2008, **47**, 283–300.
- 7 S. Manneville, *Rheol. Acta*, 2008, **47**, 301–318.
- 8 J. K. G. Dhont and W. J. Briels, *Rheol. Acta*, 2008, **47**, 257–281.
- 9 P. T. Callaghan, *Rheol. Acta*, 2008, **47**, 243–255.
- 10 P. Guenoun, R. Gastaud, F. Perrot and D. Beysens, *Phys. Rev. A: At., Mol., Opt. Phys.*, 1987, **36**, 4876–4890.
- 11 C. K. Chan, F. Perrot and D. Beysens, *Phys. Rev. A: At., Mol., Opt. Phys.*, 1991, **43**, 1826–1839.
- 12 T. Hashimoto, K. Matsuzaka, E. Moses and A. Onuki, *Phys. Rev. Lett.*, 1995, **74**, 126–129.
- 13 J. Lauger, C. Laubner and W. Gronski, *Phys. Rev. Lett.*, 1995, **75**, 3576–3579.
- 14 K. Matsuzaka, T. Koga and T. Hashimoto, *Phys. Rev. Lett.*, 1998, **80**, 5441–5444.
- 15 F. Corberi, G. Gonnella and A. Lamura, *Phys. Rev. Lett.*, 1999, **83**, 4057–4060.
- 16 Z. Y. Shou and A. Chakrabarti, *Phys. Rev. E: Stat. Phys., Plasmas, Fluids, Relat. Interdiscip. Top.*, 2000, **61**, R2200–R2203.
- 17 L. Berthier, *Phys. Rev. E: Stat. Phys., Plasmas, Fluids, Relat. Interdiscip. Top.*, 2001, **63**, 051503.
- 18 H. Lowen, *J. Phys.: Condens. Matter*, 2008, **20**, 404201.
- 19 P. Stansell, K. Stratford, J. C. Desplat, R. Adhikari and M. E. Cates, *Phys. Rev. Lett.*, 2006, **96**, 085701.
- 20 K. Stratford, J.-C. Desplat, P. Stansell and M. Cates, *Phys. Rev. E: Stat., Nonlinear, Soft Matter Phys.*, 2007, **76**, 030501.
- 21 S. M. Fielding, *Phys. Rev. E: Stat., Nonlinear, Soft Matter Phys.*, 2008, **77**, 021504.
- 22 M. Doi and A. Onuki, *J. Phys. II*, 1992, **2**, 1631–1656.
- 23 S. T. Milner, *Phys. Rev. E: Stat. Phys., Plasmas, Fluids, Relat. Interdiscip. Top.*, 1993, **48**, 3674–3691.
- 24 H. Ji and E. Helfand, *Macromolecules*, 1995, **28**, 3869–3880.
- 25 N. Clarke and T. C. B. McLeish, *Phys. Rev. E: Stat. Phys., Plasmas, Fluids, Relat. Interdiscip. Top.*, 1998, **57**, R3731–R3734.
- 26 S. M. Fielding and P. D. Olmsted, *Phys. Rev. Lett.*, 2003, **90**, 224501.
- 27 L. Jupp, T. Kawakatsu and X. F. Yuan, *J. Chem. Phys.*, 2003, **119**, 6361–6372.
- 28 S. M. Fielding and P. D. Olmsted, *Phys. Rev. Lett.*, 2006, **96**, 104502.
- 29 X.-W. Guo, S. Zou, X. Yang, X.-F. Yuan and M. Wang, *RSC Adv.*, 2014, **4**, 61167–61177.
- 30 R. Keunings, *Rheol. Rev.*, 2004, **2004**, 67–98.
- 31 M. Hulsen, A. Van Heel and B. Van Den Brule, *J. Non-Newtonian Fluid Mech.*, 1997, **70**, 79–101.
- 32 H. Åttinger, B. Van Den Brule and M. Hulsen, *J. Non-Newtonian Fluid Mech.*, 1997, **70**, 255–261.
- 33 X. J. Fan, N. Phan-Thien and R. Zheng, *J. Non-Newtonian Fluid Mech.*, 1999, **84**, 257–274.
- 34 M. Bajaj, P. P. Bhat, J. R. Prakash and M. Pasquali, *J. Non-Newtonian Fluid Mech.*, 2006, **140**, 87–107.
- 35 Z. M. Lu, B. C. Khoo, H. S. Dou, N. Phan-Thien and K. S. Yeo, *Chem. Eng. Sci.*, 2006, **61**, 4998–5009.
- 36 X. Y. Xu, J. Ouyang, W. M. Li and Q. S. Liu, *J. Non-Newtonian Fluid Mech.*, 2014, **208**, 59–71.
- 37 T. N. Phillips and K. D. Smith, *J. Non-Newtonian Fluid Mech.*, 2006, **138**, 98–110.
- 38 C. Mangoubi, M. A. Hulsen and R. Kupferman, *J. Non-Newtonian Fluid Mech.*, 2009, **157**, 188–196.
- 39 M. Griebel and A. Ruttgers, *J. Non-Newtonian Fluid Mech.*, 2014, **205**, 41–63.
- 40 A. Onuki, *J. Phys.: Condens. Matter*, 1997, **9**, 6119.
- 41 L. Jupp and X. F. Yuan, *J. Non-Newtonian Fluid Mech.*, 2004, **124**, 93–101.
- 42 M. Cromer, M. C. Villet, G. H. Fredrickson and L. G. Leal, *Phys. Fluids*, 2013, **25**, 051703.
- 43 S. C. Omowunmi and X. F. Yuan, *Rheol. Acta*, 2013, **52**, 337–354.
- 44 C. Chauviere and A. Lozinski, *J. Non-Newtonian Fluid Mech.*, 2004, **122**, 201–214.
- 45 A. Lozinski and U. Chauviere, *J. Comput. Phys.*, 2003, **189**, 607–625.
- 46 P. C. Sousa, P. M. Coelho, M. S. N. Oliveira and M. A. Alves, *Chem. Eng. Sci.*, 2011, **66**, 998–1009.
- 47 H. Tanaka, *J. Chem. Phys.*, 1994, **100**, 5323–5337.
- 48 H. Tanaka, *J. Chem. Phys.*, 1996, **105**, 10099–10114.